# CNN-based Deblurring of Terahertz Images

Marina Ljubenović[a], Shabab Bazrafkan[b], Jan De Beenhouwer[c] and Jan Sijbers[d]
*imec-Vision Lab, Department of Physics, University of Antwerp, Belgium*
{*marina.ljubenovic, shabab.bazrafkan, jan.debeenhouwer, jan.sijbers*}*@uantwerpen.be*

Keywords: THz Imaging, THz-TDS, CNN, Deblurring.

Abstract: The past decade has seen a rapid development of terahertz (THz) technology and imaging. One way of doing THz imaging is measuring the transmittance of a THz beam through the object. Although THz imaging is a useful tool in many applications, there are several effects of a THz beam not fully addressed in the literature such as reflection and refraction losses and the effects of a THz beam shape. A THz beam has a non-zero waist and therefore introduces blurring in transmittance projection images which is addressed in the current work. We start by introducing THz time-domain images that represent 3D hyperspectral cubes and artefacts present in these images. Furthermore, we formulate the beam shape effects removal as a deblurring problem and propose a novel approach to tackle it by first denoising the hyperspectral cube, followed by a band by band deblurring step using convolutional neural networks (CNN). To the best of our knowledge, this is the first time that a CNN is used to reduce the THz beam shape effects. Experiments on simulated THz images show superior results for the proposed method compared to conventional model-based deblurring methods.

## 1 INTRODUCTION

Terahertz (THz) technology, and especially THz imaging has attracted increasing interest in recent years, mostly due to immense progress in THz sources development (Guillet et al., 2014). Many imaging applications in security (Kemp et al., 2003), conservation of cultural heritage (Cosentino, 2016), and in many other fields, find their place within a THz range (i.e., 0.1 to 10 THz). Additionally, such increasing interest is attributed to the fact that a THz beam is non-ionizing and can be applied to soft materials providing an alternative to X-ray in many applications (e.g., computed tomography (CT) (Recur et al., 2012)). Moreover, THz technology is used in spectroscopy for testing, imaging, analysing, and chemical recognition of different materials (Baxter and Guglietta, 2011).

While in recent years powerful THz detectors have been developed and applied to imaging (El Fatimy et al., 2009), they are not yet fully integrated with an array structure (Nadar et al., 2010; Burger et al., 2019). Current detectors are usually one- to few-pixels large, leading to a long scanning time as for 2D images, an object needs to be scanned pixel by pixel. Secondly, the propagation of a THz beam through the object leads to the diffraction effect (Mukherjee et al., 2013) and Fresnel losses (Tepe et al., 2017). Finally, the effects of a THz beam shape additionally limit the achievable resolution. These effects cannot be neglected as the THz beam has a non-zero waist (minimum beam radius) and therefore introduces a blurring effect to the resulting image.

In recent years, several methods were proposed to deal with the afore mentioned blurring effects and to increase the spatial resolution of THz images. In (Xu et al., 2014b), the authors employed several well-known super-resolution approaches to THz images: projection onto a convex set, iterative backprojection, Richardson–Lucy iterative approach (Richardson, 1972; Lucy, 1974), and 2D wavelet decomposition reconstruction (Mallat, 2008). In (Popescu and Hellicar, 2010), a method is presented for a point-spread function (PSF) estimation by applying a specially designed phantom. To validate PSF estimation, they perform several experiments applying a well-known Wiener deconvolution technique (Dhawan et al., 1986). To deal with THz beam shape effects in THz-CT, Recur *et al.* modelled a THz beam and incorporated it in several well-established CT reconstruction approaches as a convolution filter (Recur et al., 2012). Although these methods yield promis-

[a] https://orcid.org/0000-0002-4404-3630
[b] https://orcid.org/0000-0003-4561-7250
[c] https://orcid.org/0000-0001-5253-1274
[d] https://orcid.org/0000-0003-4225-2487

ing results, they are tailored to a single THz image or a specific application (e.g., THz-CT). Furthermore, conventional deconvolution approaches require one or more input parameters that, in many cases, need to be hand-tuned.

In this work, we propose a method for beam shape effects removal from time-domain THz images that represent a hyperspectral cube with several hundred bands. The problem of beam shape effects removal can be formulated as a deblurring task, also known as deconvolution, with a known, band-dependant, PSF. In fact, a cross-section of a THz beam at the object position can be modelled as a Gaussian distribution (Recur et al., 2012).

In the last few years, we are witnessing the rapid development of deep learning and neural network-based approaches for various computer vision tasks (LeCun et al., 2015; Voulodimos et al., 2018). The convolutional neural network (CNN) is arguably the most common class of deep neural networks applied to image restoration tasks, such as denoising (Zhang et al., 2017) and deblurring (Xu et al., 2014a). Here, we will show how a CNN-based deblurring approach tailored to THz images can be applied to remove the blurring effect of a Gaussian beam. By using CNN-based deblurring, we avoid hand-tuning of the input parameters as network weights can be learned from a set of training images.

In Section 2, we start by introducing a pulsed/time-domain THz system and show how the time-domain THz images can be synthesized using different artefacts (e.g., blur and noise). We also explain how the THz beam is typically modelled and parameterized and finally introduce a novel CNN-based approach for removing its effects. Finally, we compare results obtained by conventional approaches with the proposed CNN-based method and demonstrate robustness to noise of the proposed approach. To the best of our knowledge, this is the first time that a CNN or any other deep learning approach is applied to deblur THz time-domain images.

# 2 THZ BEAM SHAPE EFFECTS

In this work, we consider only a pulsed/time-domain THz system, and, therefore, we will briefly introduce it in this section.

## 2.1 Time-domain THz Imaging

THz time-domain spectroscopy (THz-TDS) is a technique that can be used for spectroscopy and imaging in the THz domain (Hu and Nuss, 1995). A typical THz-TDS system employs an ultrashort pulsed laser (with pulses duration of 1 ps or less) and an antenna (e.g., low-temperature grown GaAs). The laser generates a series of pulses which is split into two halves: one for THz generation and the second to gate a detector. A THz detector receives the incoming radiation only for very brief periods of time which leads to sampling of the THz field at various delays. Finally, the resulting pulse is transformed into the frequency domain covering a broad range of frequencies (e.g., from 0.076 to 2 THz). For more information about the THz-TDS system and beamforming we refer to (Chan et al., 2007) and references therein.

The main advantage of THz-TDS is its ability to measure both spectral amplitude and phase. The amplitude of a THz signal is correlated to the absorbtion and the phase is correlated to the thickness and density of the scanned object. Another unique characteristic of THz-TDS is the broad bandwidth of the THz radiation which is valuable for spectroscopy as many materials have a unique fingerprint in the THz domain (Baxter and Guglietta, 2011). Furthermore, in order to be suitable for imaging and to increase the spatial resolution, an imaging system typically includes focusing optics. Finally, an image is formed from the full dataset which contains a complete THz time-domain waveform, the amplitude and the phase, corresponding to each pixel of the image. Additionally, we may choose to calculate transmittance and phase-difference images by measuring a reference background by leaving the optical path open. The resulting THz-TDS images is seen as a hyperspectral data cube where every band represents an image on a different frequency in a given range.

With the introduction of the focusing optics, the focal spot of the THz beam at the place of the object has a complicated characteristic which strongly depends on its design and system frequencies. Images formed from lower frequencies are more blurry as the beam waist increases with decreasing frequency. The high frequency bands on the other hand are less blurry because of the smaller beam waist. However, these high frequency bands are noisier as they have lower amplitudes (Duvillaret et al., 2000). Figure 1 shows three bands of a real amplitude THz-TDS image of a leaf acquired in a transmittance mode (a THz beam is transmitted through the object).

## 2.2 THz Beam Modelling

In THz-TDS imaging, the THz beam can be modelled as a Gaussian distribution characterized by a beam waist which is closely connected to a frequency of the THz system (Recur et al., 2012). Following the

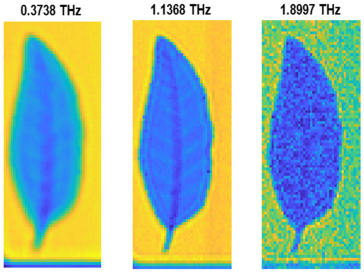


Figure 1: The THz-TDS amplitude image of a leaf at different frequencies: left - 0.3738 THz (more blurry); middle - 1.1368 THz; right - 1.8997 THz (more noisy).

general beam modelling formulation, the radius at the position $x$ from the beam waist $w_0$ is

$$w(x) = w_0\sqrt{1+(\frac{x}{x_R})^2}, \tag{1}$$

where $x_R = \frac{\pi w_0^2}{\lambda}$ is the Rayleigh range with $\lambda$ representing a wavelength. Furthermore, if $I_0$ represents the beam intensity at the centre of $w_0$ and $y$ and $z$ are distances from the beam axes in two directions, the intensity distribution over cross-section in 3D is modelled as

$$I(x,y,z) = I_0\Big(\frac{w_0}{w(x)}\Big)^2 \exp\Big(\frac{-2(y^2+z^2)}{w^2(x)}\Big). \tag{2}$$

We model the blurring artefacts present in one band of THz-TDS images as the convolution between an underlying sharp image and a known PSF

$$g = f \circledast h + n, \tag{3}$$

where $g$, $f$, $h$, and $n$ represent one band of an observed THz-TDS image, one band of an unknown sharp image, a PSF (blurring operator), and noise respectively. $\circledast$ represents the convolution operator. Our goal is to estimate the underlying sharp image $f$.

From (2) it is clear that several parameters define the intensity within the beam: the wavelength ($\lambda$), the beam waist ($w_0$), and the intensity of the beam at $w_0$ ($I_0$). We can set these parameters to control a PSF model $h$ which is used as a known variable in (3). Note that the PSF represents an intersection of the 3D THz beam in a position of the scanned object (see Figure 2).

The main goal of this work is to remove the blurring effects from THz-TDS images. This is a challenging task as not only we have a different blur (PSF) for different bands but also different noise levels. Moreover, the size of each THz image band is usually small (e.g., $61 \times 41$ pixels) which additionally complicates a deblurring process. The differences in blur and noise over bands and the small image size

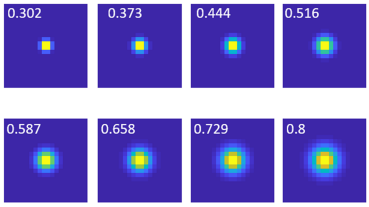


Figure 2: Influence of a beam waist on PSF: Examples of PSF for 1 THz, $I_0 = 1$, and different $w_0$ in mm (presented with the numbers in the upper-left corner).

inspired us to propose a CNN-based deblurring approach: the proposed network is learned from a training dataset which contains all of these differences and therefore it is arguably more robust than conventional deblurring approaches.

## 3 CNN-BASED DEBLURRING

In the past few years, a new Machine Learning technique known as Deep Learning influenced a wide range of experimental sciences with its revolutionary approach in solving signal processing problems (Lemley et al., 2017). The main target of deep learning includes but is not limited to solving highly nonlinear, and sophisticated image processing problems using a type of signal processing unit known as Deep Neural Networks (DNN). These models consist of different processing blocks such as fully connected, convolution and deconvolution layers and pooling and unpooling operations. DNNs provide superior results in both classification and regression problems compared to the classical machine learning approaches. Applications such as object detection and classification (Girshick, 2015; Ren et al., 2015; Redmon et al., 2016), image segmentation for both medical (Ronneberger et al., 2015) and consumer (Varkarakis et al., 2020; Badrinarayanan et al., 2017) use cases, and image acquisition and reconstruction in CT (Bazrafkan et al., 2019) are a few examples of Deep Learning impacts on modern solutions for Image Processing applications.

In the current study, a fully convolutional DNN is utilized to perform the deblurring operation to THz images. A fully convolutional network only consists of convolution and/or deconvolution layers with or without pooling operations. All layers perform the convolution operation with a learnable kernel which is given by:

$$S^m(x,y,c) = \sigma\Big(\sum_{k=1}^{n_c^{m-1}} \sum_{j=-\lfloor n_w/2 \rfloor}^{\lfloor n_w/2 \rfloor} \sum_{i=-\lfloor n_h/2 \rfloor}^{\lfloor n_h/2 \rfloor} H_c^m(i,j,k) \cdot S^{m-1}(x-i, y-j, k)\Big), \tag{4}$$

where $S^m(i,j,c)$ is the signal in pixel location $(x,y)$, located in channel $c$ in layer $m$, $H_c^m$ is the kernel associated with the channel $c$ of layer $m$. In other words this kernel maps every channel in layer $m-1$ to channel $c$ in layer $m$. $n_h$ and $n_w$ are the width and height of the kernel and $n_c^{m-1}$ is number of channels in layer $m-1$. $\sigma$ is the activation function which is also known as the nonlinearity of the layer.

In (Xu et al., 2014a), the authors proposed a network architecture designed for image deblurring. This network is shown in Figure 3. The first two layers consist of horizontal and vertical kernels and the last layer performs convolution with a large square kernel. This design resembles the Singular Value Decomposition (SVD) technique used in conventional deblurring methods, with the difference that here these filters could be learned during training.

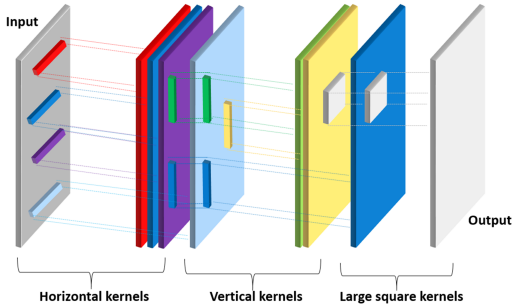


Figure 3: THzNet-2D architecture.

There are several other approaches for utilizing DNNs to perform image deblurring (Tao et al., 2018; Zhang et al., 2018). Nevertheless, we choose to use the approach from (Xu et al., 2014a) as the proposed network design is supported by the model-based method (i.e., SVD) commonly used for image restoration and therefore well studded.

# 4 EXPERIMENTS

To train and test a network, we created in total 8000 training and 200 test images corrupted by Gaussian and Poisson noise and different blurs. We used these two noise types to make the CNN more robust as THz-TDS images in practice may be corrupted by noise from several sources (Duvillaret et al., 2000). Synthetic THz-TDS images (size: $61 \times 41 \times 263$ pixels) are created by corrupting bands with different blurs (controlled by different $w_0$ and $\lambda$ as described by Eq. (1)) and noise levels to simulate images as described in Subsection 2.1. Frequencies over bands (and therefore corresponding $\lambda$) are always set from 0.0076 to 1.9989 THz. The beam waists $w_0$ and input noise levels over bands are randomly chosen from sets presented in Table 1.

Table 1: Variations of $w_0$, noise level for Gaussian noise, and noise level for Poisson noise.

| $w_0$ [mm] | Gaussian | Poisson (SNR) |
|---|---|---|
| 1.5 - 0.5 | 0 | 68 - 13 dB |
| 1.8 - 0.5 | 0 - 0.1 | 70 - 15 dB |
| 1.5 - 0.3 | 0 - 0.2 | 72 - 17 dB |
| 1.7 - 0.4 | 0 - 0.4 | 74 - 19 dB |

The proposed approach contains two steps: in the first step, we perform denoising as preprocessing followed by the second step, CNN-based deblurring. Denoising is performed using a state-of-the-art hyperspectral image denoiser FastHyDe (Zhuang and Bioucas-Dias, 2018) tailored to both Gaussian and Poisson noise. Deblurring is performed band by band, namely input and output of THzNet-2D is an image corresponding to one band of a THz-TDS cube.

An ADAM optimizer (Kingma and Ba, 2014) was utilized to update the network parameters with learning rate, $\beta_1$, $\beta_2$ and $\varepsilon$ equal to 0.00001, 0.9, 0.999, and $10^{-8}$, respectively. The MXNET 1.3.0 (Chen et al., 2015) [1] framework was used to train the network on a NVIDIA GTX 1070 in all the experiments.

To find optimal network settings we varied the number and texture of training data and the approach to weights initialization. These variations are listed in Table 2. Note that in Table 2, 6k_r stands for 6000 training images (6k THz-TDS cubes) from which 4k is without texture and 2k is with background texture that is extracted from real THz-TDS images. Similarly, THzNet-2D-6k_t contains 4k training data without texture and 2k with synthetic texture (e.g., stripes, dots). In every experiment, 20% of training images are used for validation. Comparison of the variations of THzNet-2D from Table 2 in terms of PSNR is shown in Figure 4.

Table 2: THzNet-2D variations. NoI: Number of training images; Init: Weights initialization method.

| THzNet-2D | NoI | Texture | Init |
|---|---|---|---|
| 1k | 1000 | No | Uniform |
| 2k | 2000 | No | Uniform |
| 4k | 4000 | No | Uniform |
| 6k_r | 6000 | Yes | Uniform |
| 6k_t | 6000 | Yes | Uniform |
| 4k_x | 4000 | No | Xavier |

Figure 4 shows the effect of the number and structure of a training data (note that the experiments are

[1] https://mxnet.apache.org/

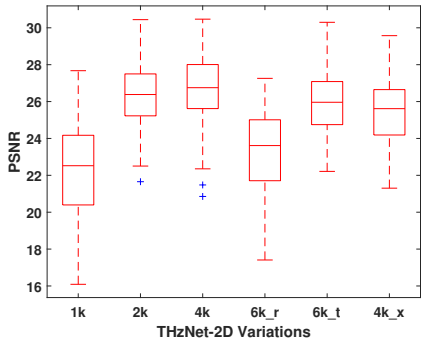


Figure 4: Comparison of different variations of THzNet-2D (PSNR values obtained on the last band).

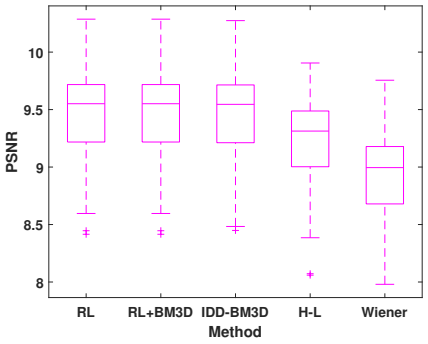


Figure 5: Comparison of conventional model-based deblurring approaches (deblurring results obtained on the last band).

performed on the last band). Firstly, we can see how the number of training data influnces the results (see the results for THzNet-2D-4k compared to THzNet-2D-2k). Secondly, the introduction of training data with additional texture does not necessarily have a positive influence on the results even if a test dataset contains both images with and without texture. Finally, we tested the influence of a different initialization approach for network weights, a so-called Xavier method (Glorot and Bengio, 2010) compared to the uniform initialization.

Furthermore, we compared our THzNet-2D network to conventional model-based deblurring/deconvolution approaches: 1) Richardson-Lucy method (RL) (Richardson, 1972; Lucy, 1974); 2) RL followed by a state-of-the-art denoiser, BM3D (Dabov et al., 2007) (RL+BM3D); 3) an extension of BM3D for non-blind deblurring, IDD-BM3D (Danielyan et al., 2012); 4) a state-of-the-art deblurring method with a hyper-Laplacian image prior (H-L) (Krishnan and Fergus, 2009); and a well-known Wiener deconvolution technique (Wiener) (Dhawan et al., 1986).

The conventional methods were tested on 100 synthetic THz-TDS images. Deblurring of THz-TDS images was performed band-by-band. Same as previously, we applied a noise removal step using FastHyDe method before deblurring. Furthermore, we chose optimal parameters for all conventional deblurring approaches by measuring *mean squared error* (MSE) and *peak signal-to-noise ratio* (PSNR). Results in terms of PSNR obtained with the model-based deblurring approaches applied to the last band (band 263) of 100 THz-TDS test images are presented in Figure 5.

Figure 5 shows that RL, RL+BM3D, and IDD-BM3D give the best results. These approaches are not imposing a prior tailored to natural images: RL is searching for a maximal likelihood solution without the use of any prior knowledge and BM3D and IDD-BM3D are based on self-similarity of non-local image patches. Here, we argue that this self-similarity is present in THz images. On the contrary, the H-L method imposes a hyper-Laplacian prior on image gradients tailored to natural images. The Wiener method expects an input parameter, noise-to-signal power ratio, which is very difficult to tune for images corrupted by moderate to strong noise.

Furthermore, in Figure 6 we show the difference in performance of the RL method and THzNet-2D-4k for different bands (namely bands 50, 100, 150, 200, and 263) and 100 THz-TDS images. We choose RL and THzNet-2D-4k as they are arguably the best tested model-based and CNN-based methods respectively. Moreover, the average difference in performance for the last band of the same 100 images measured by three metrics, MSE, PSNR, and *structural similarity index* (SSIM) is shown in Table 3.

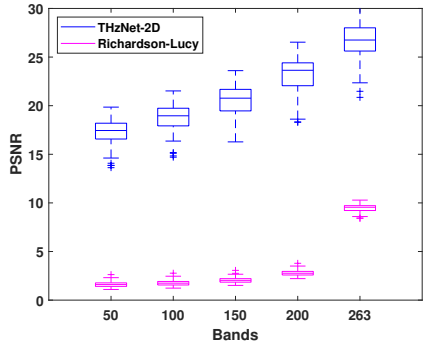


Figure 6: THzNet-2D vs Richardson-Lucy in terms of PSNR for different bands (50, 100, 150, 200, and 263).

Table 3: THzNet-2D vs Richardson-Lucy.

| Method | MSE | PSNR | SSIM |
|---|---|---|---|
| RL | 0.113 | 9.475 | 0.544 |
| THzNet-2D | **0.002** | **26.673** | **0.929** |

Figure 6 and Table 3 show that THzNet-2D outperforms significantly the model-based method for several tested bands. We also see that for higher bands there is a better performance which is expected as they are less blurry and the noise is mostly removed during preprocessing.

Figure 7 illustrates the performance of THzNet-2D for bands 50, 150, and 263. The first column shows the ground truth bands and the second column represents the same bands with added blur and noise. Furthermore, in the third column, we show the results after preprocessing/denoising and finally, the fourth and fifth columns show results obtained by the RL method and THzNet-2D, respectively. The results obtained by the RL method indicates strong ringing and boundary artefacts. Boundary artefacts are most likely due to the incorrect assumption of cyclic convolution in (3). THzNet-2D output bands do not suffer from the same artefacts. Nevertheless, we see that for the lower band (band 50), the network output shows some missing pixels especially visible on squared objects. Note that these square objects are only one pixel thick.

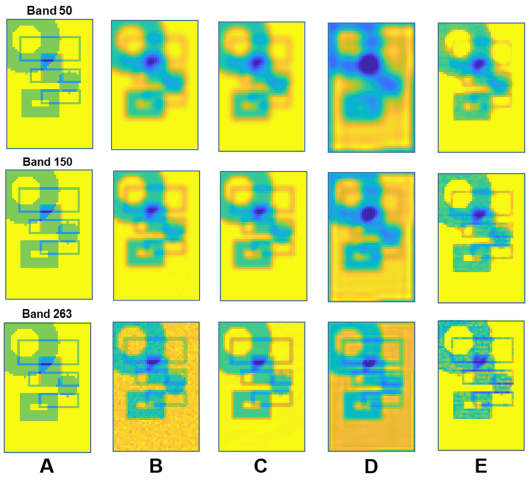


Figure 7: THzNet-2D visual results for bands 50, 150, and 263 (first, second, and third rows respectively): A: Ground truth; B: Blurry and noisy THz-TDS image; C: Blurry denoised THz-TDS image (THzNet-2D input); D: RL estimation; E: THzNet-2D output.

To show the influence of texture on deblurring results, we tested THzNet-2D on an image without any texture and with added texture pattern. Figure 8 shows the texture pattern and the obtained results. In the first row, we see the original ground truth image without texture (A), followed by the texture pattern (B), and the ground truth image with the added pattern (C). Note that the contrast in the image C is increased for the illustration purpose. The second row represents the THzNet-2D output obtained on the last band of the two THz-TDS images synthesized from the above ground truths (D and E). The network outputs are comparable with the small differences visible near the object edges.

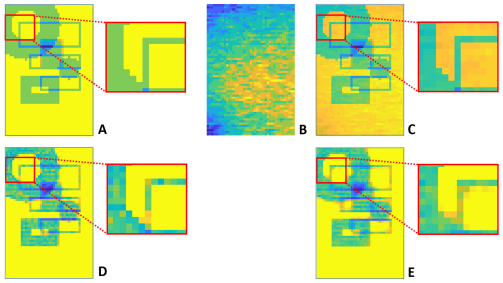


Figure 8: Influence of texture on deblurring results. A: Ground truth without texture; B: added texture pattern; C: Ground truth with texture; D: THzNet-2D output tested on image A (band 263); E: THzNet-2D output tested on image C (band 263).

Finally, to test robustness to noise, we tested THzNet-2D on images corrupted originally by Poisson noise with different noise levels (i.e., SNR of the last band is from 29 to 13 dB). Although, the noise is mostly removed during preprocessing it is interesting to see its influence on the network performance. Figure 9 shows that the network performance decreases only for very high noise levels (e.g., SNR = 15 and 13 dB). To emphasize this result, in Figure 10, we illustrate THzNet-2D output of the last band for different input noise levels.

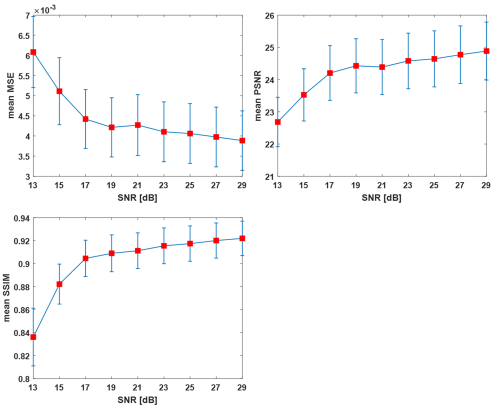


Figure 9: Robustness to noise: Mean MSE, PSNR, and SSIM for the last band of 100 test images. The $x$ axis is the Poisson noise SNR in dB.

## 5 CONCLUSION

In this work, we propose a novel CNN-based approach for deblurring THz-TDS images. We showed the superiority of the proposed method tested on syn-

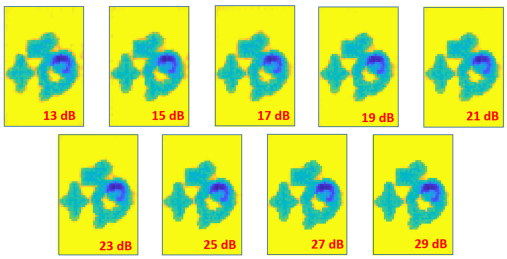


Figure 10: Robustness to noise: THzNet-2D output visual results. Input noise levels in dB presented with numbers in the bottom-right corner.

thetic images and compared to conventional model-based deblurring methods in performing 2D-based deblurring. There are several reasons for choosing CNN-based approach, to name only two: i) CNNs are robust to small-size and low-resolution images and ii) there is no need for parameter settings as the network weights are learned from training data. A drawback of the proposed THzNet-2D network is reflected in the process of creating realistic and sufficient training data. That is, training images need to resemble real THz-TDS images as close as possible in terms of size, artefacts (e.g., blur and noise), texture, and intensity levels. Therefore, our current work covers creating more complex intensity patterns and more realistic training data. This is an important task as it will provide a step towards testing the proposed CNN-based approach on real data. Nevertheless, the proposed CNN-based deblurring method can be seen as a proof of concept: we show that employing a neural network-based approach improve deblurring results significantly.

Finally, there are at least two possible extensions of THzNet-2D. The first one, covered by our current work, is an extension of the network to perform deblurring on all bands jointly. By doing this, the network may be able to learn connections between bands during training. The second extension will include denoising into a deblurring process: instead of performing denoising as preprocessing, the network should learn to perform both tasks denoising and deblurring.

## ACKNOWLEDGEMENTS

The research leading to these results was part of the IMEC-B-budget Tera-Tomo project (project number 41672). We thank Pavel Paramonov from Visan Lab for fruitful discussions. We also thank Bert Gyselinckx and Lei Zhang from imec USA and Sachin Kasture, Roelof Jansen, and Xavier Rottenberg from imec for discussions and help with data acquisition.

## REFERENCES

Badrinarayanan, V., Kendall, A., and Cipolla, R. (2017). Segnet: A Deep Convolutional Encoder-Decoder Architecture for Image Segmentation. *IEEE Transactions on Pattern Analysis and Machine Intelligence*, 39(12):2481–2495.

Baxter, J. B. and Guglietta, G. W. (2011). Terahertz Spectroscopy. *Analytical Chemistry*, 83(12):4342–4368.

Bazrafkan, S., Van Nieuwenhove, V., Soons, J., De Beenhouwer, J., and Sijbers, J. (2019). Deep Neural Network Assisted Iterative Reconstruction Method for Low Dose CT. *arXiv preprint arXiv:1906.00650*.

Burger, M., Föcke, J., Nickel, L., Jung, P., and Augustin, S. (2019). *Reconstruction Methods in THz Single-Pixel Imaging*, pages 263–290. Springer International Publishing, Cham.

Chan, W. L., Deibel, J., and Mittleman, D. M. (2007). Imaging with Terahertz Radiation. *Reports on Progress in Physics*, 70(8):1325–1379.

Chen, T., Li, M., Li, Y., Lin, M., Wang, N., Wang, M., Xiao, T., Xu, B., Zhang, C., and Zhang, Z. (2015). Mxnet: A Flexible and Efficient Machine Learning Library for Heterogeneous Distributed Systems. *arXiv preprint arXiv:1512.01274*.

Cosentino, A. (2016). Terahertz and Cultural Heritage Science Examination of Art and Archaeology. *Technologies*, 4(1):1–13.

Dabov, K., Foi, A., Katkovnik, V., and Egiazarian, K. (2007). Image Denoising by Sparse 3-D Transform-Domain Collaborative Filtering. *IEEE Transactions on Image Processing*, 16(8):2080–2095.

Danielyan, A., Katkovnik, V., and Egiazarian, K. (2012). BM3D Frames and Variational Image Deblurring. *IEEE Transactions on Image Processing*, 21(4):1715–1728.

Dhawan, A., Rangayyan, R., and Gordon, R. (1986). Image Restoration by Wiener Deconvolution in Limited-View Computed Tomography. *Applied optics*, 24(23):4013.

Duvillaret, L., Garet, F., and Coutaz, J.-L. (2000). Influence of Noise on the Characterization of Materials by Terahertz Time-Domain Spectroscopy. *Journal of the Optical Society of America B*, 17(3):452–461.

El Fatimy, A., Delagnes, J.-C., Younus, A., Nguema, E., Teppe, F., Knap, W., Abraham, E., and Mounaix, P. (2009). Plasma Wave Field Effect Transistor as a Resonant Detector for 1 Terahertz Imaging Applications. *Optics Communications*, 282(15):3055–3058.

Girshick, R. (2015). Fast R-CNN. In *Proceedings of the IEEE International Conference on Computer Vision*, pages 1440–1448.

Glorot, X. and Bengio, Y. (2010). Understanding the Difficulty of Training Deep Feedforward Neural Networks. In *AISTATS*, volume 9 of *JMLR Proceedings*, pages 249–256.

Guillet, J. P., Recur, B., Frederique, L., Bousquet, B., Canioni, L., Manek-Hönninger, I., Desbarats, P., and Mounaix, P. (2014). Review of Terahertz Tomogra-

phy Techniques. *Journal of Infrared, Millimeter and Terahertz Waves*, 35(4):382–411.

Hu, B. B. and Nuss, M. C. (1995). Imaging with Terahertz Waves. *Optics Letters*, 20(16):1716–1718.

Kemp, M. C., Taday, P. F., Cole, B. E., Cluff, J. A., Fitzgerald, A. J., and Tribe, W. R. (2003). Security Applications of Terahertz Technology. In *Terahertz for Military and Security Applications*, volume 5070, pages 44–52.

Kingma, D. P. and Ba, J. (2014). Adam: A Method for Stochastic Optimization. *arXiv preprint arXiv:1412.6980*.

Krishnan, D. and Fergus, R. (2009). Fast Image Deconvolution using Hyper-Laplacian Priors. In *Advances in Neural Information Processing Systems*, pages 1033–1041.

LeCun, Y., Bengio, Y., and Hinton, G. E. (2015). Deep Learning. *Nature*, 521(7553):436–444.

Lemley, J., Bazrafkan, S., and Corcoran, P. (2017). Deep Learning for Consumer Devices and Services: Pushing the limits for machine learning, artificial intelligence, and computer vision. *IEEE Consumer Electronics Magazine*, 6(2):48–56.

Lucy, L. B. (1974). An Iterative Technique for the Rectification of Observed Distributions. *The Astronomical Journal*, 79(6):745–754.

Mallat, S. (2008). *A Wavelet Tour of Signal Processing, Third Edition: The Sparse Way*. Academic Press, Inc., Orlando, FL, USA, 3rd edition.

Mukherjee, S., Federici, J., Lopes, P., and Cabral, M. (2013). Elimination of Fresnel Reflection Boundary Effects and Beam Steering in Pulsed Terahertz Computed Tomography. *Journal of Infrared, Millimeter, and Terahertz Waves*, 34(9):539–555.

Nadar, S., Videlier, H., Coquillat, D., Teppe, F., Sakowicz, M., Dyakonova, N., Knap, W., Seliuta, D., and Kašalynas, I. (2010). Room Temperature Imaging at 1.63 and 2.54 THz with Field Effect Transistor Detectors. *Journal of Applied Physics*, 108(5):054508.

Popescu, D. C. and Hellicar, A. D. (2010). Point Spread Function Estimation for a Terahertz Imaging System. *EURASIP Journal on Advances in Signal Processing*, 2010(1):575817.

Recur, B., Guillet, J. P., Manek-Hönninger, I., Delagnes, J. C., Benharbone, W., Desbarats, P., Domenger, J. P., Canioni, L., and Mounaix, P. (2012). Propagation Beam Consideration for 3D THz Computed Tomography. *Optics Express*, 20(6):5817–5829.

Redmon, J., Divvala, S., Girshick, R., and Farhadi, A. (2016). You Only Look Once: Unified, Real-Time Object Detection. In *Proceedings of the IEEE Conference on Computer Vision and PatternRecognition*, pages 779–788.

Ren, S., He, K., Girshick, R., and Sun, J. (2015). Faster R-CNN: Towards Real-Time Object Detection with Region Proposal Networks. In *Advances in Neural Information Processing Systems*, pages 91–99.

Richardson, W. H. (1972). Bayesian-Based Iterative Method of Image Restoration. *Journal of the Optical Society of America*, 62(1):55–59.

Ronneberger, O., Fischer, P., and Brox, T. (2015). U-Net: Convolutional Networks for Biomedical Image Segmentation. In *International Conference on Medical Image Computing and Computer-Assisted Intervention*, pages 234–241.

Tao, X., Gao, H., Shen, X., Wang, J., and Jia, J. (2018). Scale-Recurrent Network for Deep Image Deblurring. In *Conference on Computer Vision and Pattern Recognition*, pages 8174–8182.

Tepe, J., Schuster, T., and Littau, B. (2017). A Modified Algebraic Reconstruction Technique Taking Refraction Into Account with an Application in Terahertz Tomography. *Inverse Problems in Science and Engineering*, 25(10):1448–1473.

Varkarakis, V., Bazrafkan, S., and Corcoran, P. (2020). Deep Neural Network and Data Augmentation Methodology for Off-Axis Iris Segmentation in Wearable Headsets. *Neural Networks*, 121:101–121.

Voulodimos, A., Doulamis, N., Doulamis, A., and Protopapadakis, E. (2018). Deep Learning for Computer Vision: A Brief Review. *Computational Intelligence and Neuroscience*, 2018:1–13.

Xu, L., Ren, J. S. J., Liu, C., and Jia, J. (2014a). Deep Convolutional Neural Network for Image Deconvolution. In *Advances in Neural Information Processing Systems 27*, pages 1790–1798. Curran Associates, Inc.

Xu, L.-M., Fan, W., and Liu, J. (2014b). High-Resolution Reconstruction for Terahertz Imaging. *Applied Optics*, 53(33):7891–7897.

Zhang, J., Pan, J., Ren, J., Song, Y., Bao, L., Lau, R. W. H., and Yang, M. (2018). Dynamic Scene Deblurring Using Spatially Variant Recurrent Neural Networks. In *2018 IEEE/CVF Conference on Computer Vision and Pattern Recognition*, pages 2521–2529.

Zhang, K., Zuo, W., Chen, Y., Meng, D., and Zhang, L. (2017). Beyond a Gaussian Denoiser: Residual Learning of Deep CNN for Image Denoising. *IEEE Transactions on Image Processing*, 26(7):3142–3155.

Zhuang, L. and Bioucas-Dias, J. M. (2018). Fast Hyperspectral Image Denoising and Inpainting Based on Low-Rank and Sparse Representations. *IEEE Journal of Selected Topics in Applied Earth Observations and Remote Sensing*, 11(3):730–742.